

Optimisation of chromium adsorption by the Box-Behnken design method: Isothermal and kinetic study on biochar and activated carbon

Fatima-Zahra Abahdou¹, Maria Benbouzid¹, Fadimatou Ahmadou¹,
Kaoutar Najy¹, Yousra El Hamdouni^{1,2}, Najoua Labjar³,
Hamid Nasrellah⁴, Souad El Hajjaji^{1*} 

¹ Laboratory of Spectroscopy, Molecular, Modeling, Materials, Nanomaterials, Water and Environment, (LS3MNWE), Department of Chemistry, Faculty of Sciences, Mohammed V University in Rabat, Av IbnBattouta, B.P. 1014, Rabat 10000, Morocco

² IRSM Laboratoire, Institut Supérieur d'Administration de Gestion et de Génie Informatique, ISMAGI, Rabat, Morocco

³ Laboratory of Spectroscopy, Molecular, Modeling, Materials, Nanomaterials, Water and Environment, (LS3MNWE), ENSAM-Rabat, Mohammed V University in Rabat, Morocco

⁴ Higher School of Education and Training, Chouaib Doukkali University, El Jadida 24000, Morocco

ABSTRACT

The contamination of water systems by heavy metals, particularly hexavalent chromium (Cr(VI)), represents a major environmental and public health challenge. Chromium is extensively used in various industries, making its removal from wastewater crucial. This study investigates the potential of biochar (ArS BC) and activated carbon (ArS AC) derived from argan shell biomass (ArS) as sustainable adsorbents for Cr(VI) removal. ArS BC was prepared by pyrolyzing ArS at 500 °C for one hour, while ArS AC was produced through chemical activation with KOH (1:4 ratio) and thermal activation at 700 °C for one hour. The materials were characterized using FTIR, XRD, pHpzc, TGA, and BET techniques to evaluate their physicochemical properties and recycling potential. The Box-Behnken Design (BBD) within the response surface methodology (RSM) framework was applied to optimize operational parameters, including pH, adsorbent dosage, and initial Cr(VI) concentration. The optimal conditions for ArS BC were found to be pH 3, a dosage of 1 g/L, and an initial Cr(VI) concentration of 10 mg/L, resulting in a maximum adsorption capacity of 48.77%. For ArS AC, the optimal conditions were pH 3, a dosage of 0.6 g/L, and an initial Cr(VI) concentration of 50 mg/L, yielding a significantly higher maximum adsorption capacity of 91.34%. Adsorption followed the Langmuir isotherm model, with R² values of 0.99 for ArS BC and 0.999 for ArS AC. The maximum adsorption capacities were 47.62 mg/g for ArS BC and 333.33 mg/g for ArS AC. Adsorption efficiency was highly influenced by pH, and desorption of Cr(VI) using acidic reagents proved challenging. ArS AC demonstrated superior stability across multiple adsorption cycles compared to ArS BC. This study highlights the promising potential of utilizing locally available argan shell waste as an efficient, cost-effective, and environmentally sustainable material for the removal of hexavalent chromium from contaminated water, offering a viable solution for water purification in regions affected by industrial pollution.

Keywords: biochar, activated carbon, argan shell, hexavalent chromium, TGA, XRD, BET, FTIR.

INTRODUCTION

Water contamination is a critical global issue that significantly impacts human health and well-being, posing serious public health challenges [1]. Ensuring access to safe drinking

water and eradicating waterborne diseases are essential for promoting a healthy and sustainable life [2]. However, various contaminants degrade water quality, rendering it unfit for human consumption and daily use. These pollutants originate from both natural and anthropogenic

sources [3], including microbial activity, geological features, and human activities such as industrial operations, agricultural practices, poor waste management, and malfunctioning sewage systems [4, 5]. Among the diverse pollutants, heavy metals are particularly problematic due to their toxicity and tendency to bioaccumulate in living organisms, leading to severe ecological and health issues [6, 7]. Compounds such as ferric chromite, crocodite and chromic ochre contain chromium, the seventh most common element on Earth. Hexavalent and trivalent chromium Cr(VI) and Cr(III) are prevalent in waste from industries such as textiles, leather tanning and electroplating [4]. While Cr(III) is less toxic, Cr(VI) which is widely present in industrial effluents, particularly from the leather, electroplating, and textile industries [5], poses a significant threat to plants, animals, and humans due to its high toxicity and mobility. Prolonged exposure to Cr(VI) can result in severe health problems, including skin irritation, liver and kidney damage, and other systemic effects [8, 9]. The removal of heavy metals, including Cr(VI), from wastewater is a priority for environmental management. Adsorption is a widely recognized method for removing heavy metals, offering high efficiency, cost-effectiveness, and environmental sustainability. Among the studied adsorbents, biochars and activated carbons stand out due to their high performance, attributed to their large specific surface area, porosity, regeneration potential [10] and affinity for metal ions [3], [9]. Several studies have demonstrated the effectiveness of biochars derived from different biomasses, such as apple wood [1], grass residues [2], eucalyptus sawdust [6], and sugarcane bagasse [10], in removing Cr(VI). Activated carbon, often derived from lignocellulosic biomass, is especially effective in wastewater treatment and is well-suited for large-scale applications. Chemical activation, particularly with KOH, is a commonly used strategy to enhance the performance of biochars by increasing their porosity and modifying their surface functional groups. For example, research has shown that KOH-activated biochar from eucalyptus sawdust exhibits enhanced adsorption capacity due to its optimized porous structure and the presence of active sites that promote Cr(VI) retention [6]. However, the efficiency of the adsorption process depends on several parameters, including pH, temperature, and particle size of the adsorbent material [11]. Also, to optimize

adsorption conditions, statistical approaches such as RSM and the Box-Behnken design have been used to determine optimal parameters and maximize Cr(VI) removal [12]. These methods enable the modeling of adsorption based on experimental variables and significantly improve process efficiency. Studies have revealed that activated biochars derived from various organic residues, such as landfill leachate sludge [7] and fruit shells [13], exhibit variable adsorption capacities depending on the experimental conditions. The particle size of the adsorbent plays a crucial role in its adsorption performance, as demonstrated in research on argan nut shell (ANS) biomass, where combustion parameters in a Stirling engine were found to be influenced by particle size [14]. The growing demand for efficient and economical adsorbents has driven interest in underutilized agricultural byproducts. *Argania spinosa*, a species native to southern Morocco, represents the country's second-largest forest, covering approximately 871,210 hectares with an annual yield of 500 kg of fruit per hectare [14]. The argan tree is not only ecologically significant but also economically vital for local communities, particularly through the production of argan oil. The processing of argan fruit generates significant quantities of argan seed shells (ArS), which remain largely unexploited, creating challenges in waste management and storage. Transforming this waste into valuable adsorbents for environmental applications offers a sustainable solution to both waste valorization and water treatment challenges. This study investigates the potential of biochar and activated carbon derived from argan seed shells for the removal of Cr(VI) from wastewater. The objectives are twofold: (1) to valorize argan seed shells as a sustainable raw material for producing biochar and activated carbon, and (2) to evaluate the efficiency of these adsorbents in removing hexavalent chromium from contaminated water through adsorption. While various agricultural byproducts have been explored for biochar production, the use of argan seed shells remains underexplored, offering a novel and sustainable approach to wastewater treatment. The findings of this study could pave the way for the development of cost-effective, environmentally sustainable water treatment technologies, particularly in arid and semi-arid regions where agricultural byproducts like argan seed shells are abundant but underutilized.

MATERIALS AND METHODS

Materials

Preparation of biochar: ArS BC

Argan shells (ArS), were initially purified using distilled water and air-dried. The shells were then crushed into fragments using a Retsch RM 200 mortar grinder, followed by sieving, to obtain particles with diameters between 630 and 400 μm . These particles were then oven-dried at 105 $^{\circ}\text{C}$ for 24 hours before being subjected to pyrolysis. The pyrolysis process was carried out for 60 minutes at 500 $^{\circ}\text{C}$ in a muffle furnace under an oxygen-free environment, with a heating rate of 10 $^{\circ}\text{C}/\text{min}$.

Preparation of activated carbon derived from ArS :ArS AC

The activation of the ArS BC combines chemical and physical activation processes in a single step. Chemical activation is carried out using 50 ml of a potassium hydroxide (KOH) solution with a mass ratio of 1:4 stirred at 60 $^{\circ}\text{C}$ in a stirrer-incubator for 2 hours. Afterward, the liquid obtained is separated by filtration and the resulting KOH-activated biochar is dried for 24 hours at 105 $^{\circ}\text{C}$. For physical activation, a batch of KOH-activated biochar precursor is introduced into a muffle furnace at 800 $^{\circ}\text{C}$ with a heating rate of 10 $^{\circ}\text{C}/\text{min}$ [15], for 90 minutes [16]. The activated biochar was initially rinsed with distilled water, followed by a 5 M hydrochloric acid (HCl) solution to neutralise the pH. It was washed again with distilled water, until a neutral pH is achieved. The resulting sample was subsequently dried at 110 $^{\circ}\text{C}$ over night before storage in a hermetically sealed bottle.

Characterisation of materials

Structural analysis by FTIR and crystallinity assessment by XRD

The structural properties of the activated carbon were investigated using a JASCO Fourier transform infrared spectrometer (FTIR), which operated over a wavelength range of 4000 to 400 cm^{-1} . To assess its crystalline structure, X-ray diffraction (XRD) analysis was performed with a Shimadzu LabXRD-6100 powder diffractometer, employing a scan rate of 0.05 to 25 degrees per minute (θ).

Thermal behavior: DTA and TGA analysis

Differential thermal analysis (DTA) and thermogravimetric analysis (TGA) were carried out in both inert (nitrogen) and oxidizing (air) environments using Labsys Evo1F Setaram equipment. The thermograms were obtained at a heating rate of 10 $^{\circ}\text{C}$ per minute and a gas flow rate of 20 mL per minute.

pH measurement

The pH of the solutions was determined with a Thermo Fisher Scientific pH meter. Residual concentrations of the drug during adsorption tests were measured using a SHIMADZU UV-19000 spectrophotometer at a wavelength of 350 nm.

Determination of pH_{pzc}

Determining the charge point at zero pH is an essential characterisation technique that provides an insight into the electrostatic forces underlying the adsorption phenomenon [17]. In this study, 0.15 mg of the two supports were suspended in 50 mL NaCl (0.01 $\text{mol}\cdot\text{L}^{-1}$), and the pH was adjusted to initial values ranging from 2 to 12. After stirring the suspensions for 48 hours and subsequent filtration, the final pH was measured and $\Delta\text{pH} = (\text{pH}_f - \text{pH}_i)$ was plotted as a function of pH_i . The isoelectric point was identified as the intersection of the curve with the zero line [18]. This measure provides valuable information about the material's electronic and chemical characteristics.

Volatile matter and moisture content H(%)

The assessment of volatile compounds and moisture content is carried out in three distinct phases. First, porcelain crucibles were heated to 1000 $^{\circ}\text{C}$ for 3 hours and then allowed to cool in a desiccator. Next, a Radwag precision balance is used to measure the weight P of the crucible. Approximately 2 g of ArS is added, and total weight (P_1) is recorded. The crucible filled with ArS is then introduced in an oven at 105 $^{\circ}\text{C}$ for 24 hours, and the weight (P_2) is measured. To measure the volatile components, the cooled crucibles from the drying process are reheated at 1000 $^{\circ}\text{C}$ for 3 hours. The final weight (P_3) is recorded after final cooling is completed [13]. Equations 2 and 3 were used to determine the moisture content and volatile matter content, respectively [13].

$$H\% = \frac{P_1 - P_2}{P_1 - P} \times 100 \quad (1)$$

$$Vm = \frac{P_2 - P_3}{P_1 - P} \times 100 \quad (2)$$

Ash content

The ash content was determined by first weighing an empty crucible (m_0). Then, 1 g of biomass was added to the crucible (m_1). The mixture was heated in an oven at 800 °C until ash was obtained. The mass of the crucible and ash (m_2) was then recorded. The ash content was calculated using the formula below [13]

$$C\% = \frac{m_2 - m_0}{m_1 - m_0} \times 100 \quad (3)$$

Optimization of adsorption parameters using response surface methodology (RSM)

An experimental approach was adopted to optimize results while controlling costs and time. This method involves systematically varying the factor levels for each experiment. RSM was used to adjust the parameters, represent, and display the experimental results to identify areas of interest and determine the optimal values for each variable [19].

Experimental design and Box-Behnken methodology

Three parameters were selected to study the effect of ArS BC and ArS AC on the adsorption of chromium(VI) in aqueous solution: pH (X_1), the quantity of adsorbent (X_2) and the initial chromium concentration [Cr^{6+}] (X_3). Each parameter was evaluated at three different levels (-1, 0, +1), as specified in Table 1. Using the JMP software, the results were obtained; this tool is effective for designing experimental strategies and analyzing experimental designs. The study employed the Box-Behnken experimental design, which includes a second-order polynomial, to construct a model suitable for the phenomenon under investigation [20]. This approach allows for the examination of adsorption tests, defining correlations between variables and optimizing the process. By using the Box-Behnken method with JMP, an effective predictive model was developed, underscoring the importance of these techniques for improving

Table 1. The experimental range of Cr(VI) adsorption on adsorbent

Variable	-1	0	+1
X_1 :pH	2	4	6
X_2 :Masse	0.2	0.6	1
X_3 : $[Cr^{6+}]$ (mg/L)	10	30	50

adsorption processes [12]. The number of experiments (N) required for a three-factor Box-Behnken design (BBD) is given by the following equation:

$$N = 2(k(k - 1)) + n_0 \quad (4)$$

where: k stands for factors number of as well as n_0 represents the number of center points. For three factors ($k=3$), this will require the planning of 15 experimental trials.

The response variable is the percentage of hexavalent chromium removed from the mixture. It is calculated using the following equation:

$$R\% = \frac{C_0 - C_{eq}}{C_0} \times 100 \quad (5)$$

where: C_0 is concentrations in $t = 0$ (mg/L) and C_{eq} is concentrations in t_{eq} (mg/L); both C_0 and C_{eq} are given by the UV-visible spectrophotometer.

Batch adsorption experiments and capacity calculation

Adsorption experiments were performed by introducing a defined amount of adsorbent into a 50 mL of potassium dichromate solution at a known initial concentration. The experiments were carried out using Cr^{6+} solutions, all maintained at pH 3. The samples were agitated at 350 rpm using a Witeg shaker while the temperature was maintained at 25 °C for two hours to ensure equilibrium. Afterward, the adsorbent was removed from the solution by filtering through a 2 μ m syringe filter. The residual Cr^{6+} concentration was measured using UV-Vis spectrophotometry at a wavelength of 350 nm, with deionized water as the reference [21]. A calibration curve was developed, covering concentrations from 10 to 50 mg/L and achieving an R^2 value greater than 0.995, to establish the correlation between absorbance (Abs) and concentration (C). The adsorption capacity, denoted as q_e (mg/g), was then calculated based on Equation 6, where V represents the volume of the solution in liters, C_0 and C_f are the initial and final concentrations in mg/L, respectively, and m is the mass of the adsorbent in grams.

$$q_e = \frac{(C_0 - C_{eq})}{m} \times V \quad (6)$$

Adsorption isotherms for the Cr (VI) metal anion on ArS BC and optimal ArS AC were established by mixing 10 mg of the two supports with 50 ml of Cr (VI) solutions at different initial dye concentrations (10–50 mg/L). The mixtures were agitated at 350 rpm and maintained at 30 °C for

2 hours [22]. The adsorption capacity of Cr(VI) was calculated using the following equation:

$$qt = \frac{(C_0 - Ct)}{m} \times V \quad (7)$$

where: q_t (mg/g) represents the amount of Cr(VI) adsorbed at a specific time t (minutes), C_t (mg/L) denotes the concentration of Cr(VI) at that same time, V (L) refers to the volume of the Cr(VI) solution, and m (g) is the adsorbent mass.

Adsorption kinetic models

Adsorption kinetics are primarily controlled by the mass transfer of the dye at the interface between the solid and liquid phases. The experimental data for Cr(VI) adsorption onto ArS BC and ArS AC were modeled using two kinetic approaches: the pseudo-first-order and pseudo-second-order models. Pseudo-first-order kinetics model: this model is based on a linear relationship between the amount of solute adsorbed on the surface of the adsorbent over time. It is expressed by the following formula:

$$\text{Log}(q_e - q_t) = \text{Log}(q_e) - \frac{K_1}{2.303} t \quad (8)$$

Pseudo-second-order kinetics model: this model indicates that chemical adsorption, such as electron exchange between the adsorbate and the solid adsorbent, may be occurring. It is expressed by the following equation:

$$t/q_t = 1/K_2 q_e^2 + t/q_e \quad (9)$$

Intra-particle diffusion model: This model is employed to determine the diffusion rate in the pores using the following Weber-Morris equation :

$$q_t = K_d \times t^{1/2} + C \quad (10)$$

where: q_t is the amount of heavy metal adsorbed (mg/g) at equilibrium and at time t ; K_1 is the pseudo-first-order rate constant (min^{-1}); K_2 is the pseudo-second-order rate constant ($\text{g}/\text{mg} \cdot \text{min}$); K_d is the intra-particle diffusion rate constant ($\text{mg}/\text{g} \cdot \text{min}^{1/2}$); and C (mg/g) is a constant related to the surface concentration of the metal on the adsorbent [23].

Adsorption isotherm

Langmuir model

The Langmuir isotherm theory assumes monolayer adsorption, where each site can accommodate only one molecule at equilibrium. At

these homogeneous sites, the rate of adsorption equals the rate of desorption, with no lateral interactions between the adsorbed molecules [24]. The Cr(VI) adsorption data on ArS BC and ArS AC were analyzed using the Langmuir model, represented by the following equation:

$$\frac{1}{q_e} = \frac{1}{q_m K_L C_e} + \frac{1}{q_m} \quad (11)$$

where: q_e refers to the Cr(VI) capacity adsorption on the sorbent in mg/g, and C_e represents the concentration at equilibrium of the heavy metal in the solution, measured in mg/L. q_m and K_L correspond to the maximum adsorption capacity and the Langmuir coefficient (L/mg), which indicates the adsorption intensity, respectively. In addition, the separation factor R_L is a dimensionless constant of Langmuir model distinct by the formula below:

$$R_L = \frac{1}{1 + K_L C_0} \quad (12)$$

where: C_0 is the initial concentration of Cr(VI) and K_L is Langmuir's constant (L/mg). The R_L values indicate the type of isotherm as follows: irreversible ($R_L = 0$), favourable ($0 < R_L < 1$), linear ($R_L = 1$) or unfavourable ($R_L > 1$).

Freundlich model

The Freundlich model assumes that the adsorption phenomenon takes place in a monolayer at equilibrium and that the adsorption sites are energetically different (heterogeneous adsorption surface) [25]. The data from Cr(VI) adsorption experiments on ArS BC and ArS AC were analyzed using the Freundlich model, expressed by the following formula:

$$\text{Log } q_e = \text{Log } K_F + \left(\frac{1}{n}\right) \text{Log } C_e \quad (13)$$

where: K_F and n are the Freundlich constants.

Temkin model

The Temkin isotherm considers that the heat of adsorption for all molecules in the surface layer decreases linearly as coverage increases. This behaviour results from reduced interactions between the adsorbent and adsorbate. This model assumes a uniform distribution of surface binding energies. The Temkin equation is given as follows:

$$q_e = B_T \ln(K_T) + B_T \ln(C_e) \quad (14)$$

where: $B_T = RT/b$ (J/mol) is the Temkin constant related to the heat of sorption, K_T (L/g) is the adsorption equilibrium constant corresponding to the maximum binding energy, R is the universal gas constant, with a value of 8.314 J/mol.K [24].

Dubinin-Radushkevich

The Dubinin-Radushkevich (D–R) model considers the Gaussian energy distribution across the heterogeneous surface of the adsorbent, which allows for the identification of the adsorption mechanism. The linearized form of this model is expressed by the following equation:

$$\ln q_e = \ln q_m - \beta \mathcal{E}^2 \quad (15)$$

where: β (mol²/kJ²) is a constant related to the mean free energy change, and \mathcal{E} represents the Polanyi potential, which is calculated using the following equation:

$$\mathcal{E} = RT \ln\left(1 + \frac{1}{C_0}\right) \quad (16)$$

The adsorption energy (E) can be derived from the following equation:

$$E = \frac{1}{\sqrt{2\beta}} \quad (17)$$

In these equations, R (8.314 J/mol/K) represents the ideal gas constant, and T denotes the absolute temperature. The value of E plays a crucial role in defining the type of adsorption: E less than 8 kJ/mol

suggests physical adsorption, while a value between 8 and 16 kJ/mol indicates chemical ion-exchange or chemisorption. In this study, the mean free energy for Cr(VI) adsorption onto ArS BC and ArS AC was determined to be above 8 kJ/mol, confirming that the process as chemical adsorption [26].

RESULTS AND DISCUSSION

Materials characterization

ArS BC and ArS AC analysis via X-ray diffraction

The recorded XRD patterns of the biochar pyrolyzed at 500 °C (ArS BC) and the KOH-activated biochar (ArS AC) are shown in Figure 1. The results indicate that both materials exhibit similar diffraction patterns, suggesting comparable structural properties. Two main peaks are observed: a broad peak in the 20° to 30° range, corresponding to the (002) crystal plane index. This peak is attributed to the parallel and azimuthal alignment of aromatic carbon structures, indicating a semi-crystalline or amorphous nature [27]. A second peak in the 40° to 50° range, corresponding to the (100) diffraction plane of graphitic and hexagonal carbon structures. This peak reflects the size of the aromatic laminae within the material. The intensity of the peaks is higher for ArS BC compared to ArS AC, suggesting a more ordered structure in the biochar. These results confirm the semi-crystalline or amorphous nature of both materials, which is typical for carbon-based adsorbents derived from biomass.

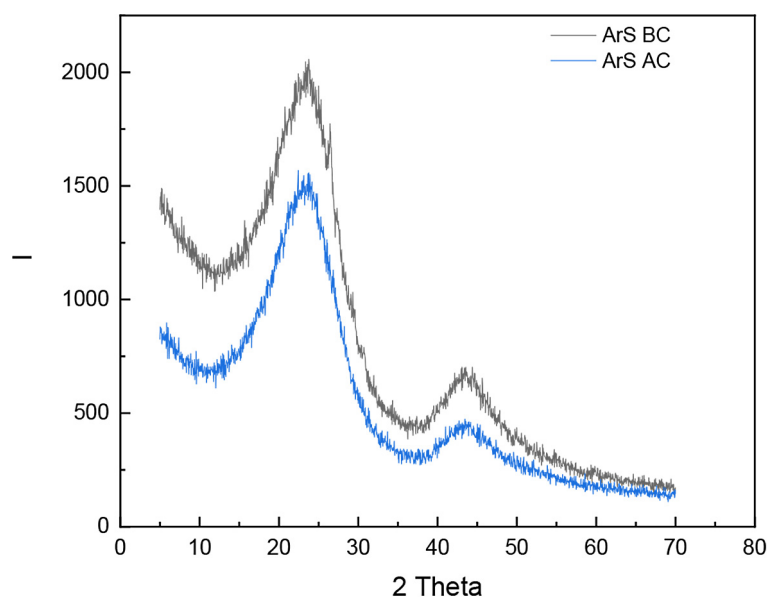


Figure 1. X-ray diffraction results of ArS AC and ArS BC

Fourier-transform infrared spectroscopy (FTIR)

FTIR spectra of the two substrates were analyzed to investigate the changes in vibrational frequencies of the functional groups present in the ArS BC before and after its activation with KOH as it is shown in Figure 2. The biomass spectra were collected over a wavenumber range of 4000 to 500 cm^{-1} .

In the FTIR spectrum of the ArS BC, notable absorption peaks were detected at various wavelengths. Specifically, a peak at 3441.83 cm^{-1} was associated with the hydroxyl functional group, while peaks at approximately 2923.7 cm^{-1} and 2857.45 cm^{-1} were identified as corresponding to the stretching vibrations of aliphatic -CH and -CH₂ groups, respectively [28]. Furthermore, a decrease in intensity was observed for the peak at 1628.36 cm^{-1} , which is linked to the C=O and C=C stretching vibrations within the aromatic ring[29]. The peak at 1384.25 cm^{-1} was ascribed to the stretching vibration of aromatic C=C. Additional peaks were noted at 1121.53 cm^{-1} and 1040.40 cm^{-1} , corresponding to C-O alkoxy and C-O aromatic stretching vibrations, respectively [29]. Additionally, a peak at 744.55 cm^{-1} was observed, which relates to the C-H stretching in benzene.

After activation with KOH, significant changes were noted. At 3435.68 cm^{-1} , the peak related to the hydroxyl group, showed broadening, while peaks at around 2926.33 cm^{-1} as well as 2862.57 cm^{-1} were attributed to aliphatic stretching vibrations -CH and -CH₂ [11]. The

intensity of the peak at 1628.26 cm^{-1} , associated with the C=O and C=C stretching vibration of the aromatic ring, was also affected[30]. At 1384.25 cm^{-1} related to the C=C aromatic stretching vibration remained present[30]. The peak at 1096.76 cm^{-1} , representing the C-O alkoxy and C-O aromatic stretching vibrations, became broader. Additionally, a peak at 764.81 cm^{-1} refers to C-H in benzene. This analysis suggests that KOH activation led to an increase in C-O surface functional groups in ArS AC compared to ArS BC.

Thermal behaviour of ArS in an inert atmosphere

Thermogravimetric analysis was employed to investigate the thermal degradation of ArS. The curves in Figure 3 below, reveal a gradual mass loss between 30 and 800 $^{\circ}\text{C}$, which can be divided into distinct stages. Both thermogravimetric (TGA) and derivative thermogravimetric (DTG) plots were obtained for ground and dried ArS. During thermogravimetric analysis under a nitrogen atmosphere at a heating rate of 10 $^{\circ}\text{C}/\text{min}$, several distinct stages were observed. A small initial mass loss (approximately 2%) occurred between 50 and 175 $^{\circ}\text{C}$, corresponding to the elimination of the moisture contained in the samples. This first stage of mass loss is endothermic [31]. Following this, a significant mass loss (around 42%) was observed between 217 and 355 $^{\circ}\text{C}$, corresponding to the hemicellulose heat degradation. A subsequent mass loss of approximately 38% occurred

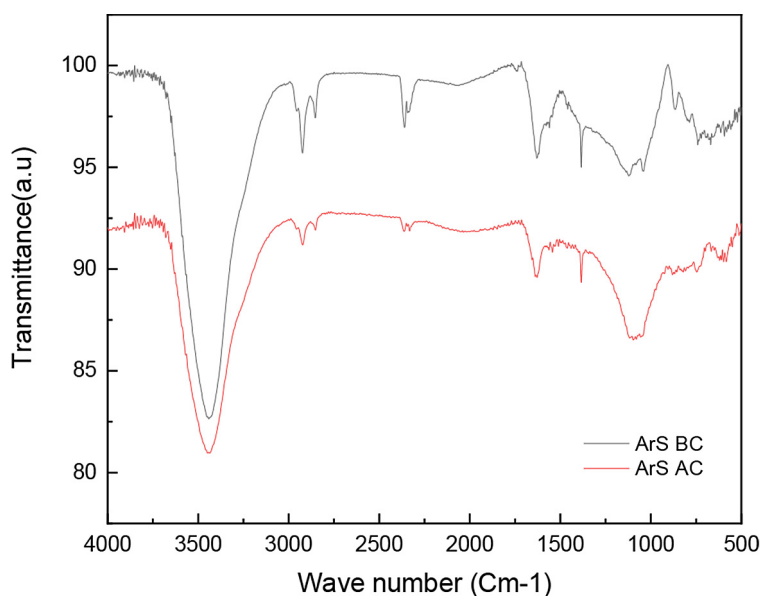


Figure 2. FTIR spectrum of ArS BC before and after activation by KOH

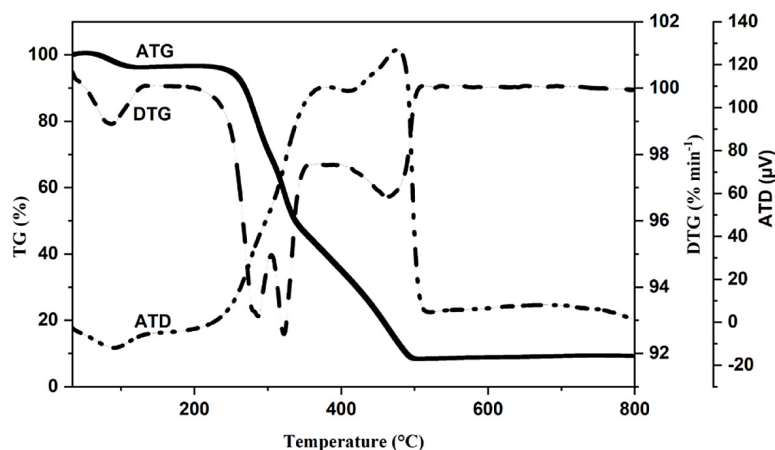


Figure 3. TG-DTG curves of ArS under pyrolysis conditions

between 336.8 and 409 °C, primarily due to the degradation of the cellulosic components present in the ArS particles [32]. Above 400 °C, this degradation generates an exothermic peak, and above 500 °C, the samples reach thermal stability, indicating their ability to produce biochar without undergoing significant transformation. The TGA analysis thus provides a detailed breakdown of the thermal decomposition stages of ArS under an inert atmosphere, providing essential information on their behaviour during the thermal conversion and biochar production processes [31].

Determination of pH_{PZC}

Determining the pH_{PZC} for ArS BC and ArS AC is important for understanding their behaviour in solution. The pH_{PZC} represents the pH at

which the net surface charge of the material is zero, with values determined to be 7.05 for ArS BC and 6.64 for ArS AC as it is shown in Figure 4 below. When the solution pH is lower than these thresholds, the surfaces of the materials become positively charged. Conversely, at pH levels exceeding these values, the surface charge shifts to negative. This characteristic is particularly relevant for the adsorption of Cr(VI) in aqueous media. Under acidic conditions, where the surfaces of ArS BC and ArS AC are positively charged, they can effectively attract anionic species. Specifically, ions such as $HCrO_4^-$, CrO_4^{2-} and $Cr_2O_7^{2-}$, which generally predominate in water when the concentration of Cr^{6+} is inferior than 1 g/L, can be effectively eliminated by the adsorption process[33].

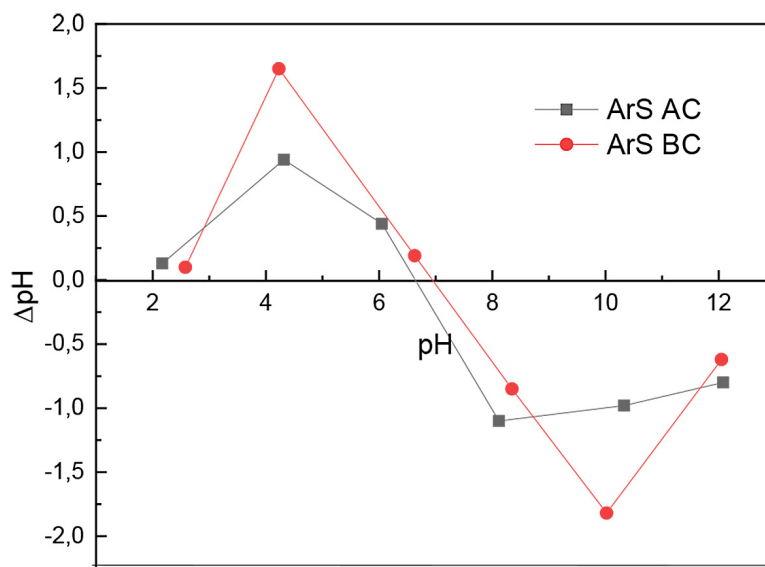


Figure 4. Determination of the pH_{PZC} values for ArS BC and ArS AC

Chemical characterization

The chemical characterization of ArS is summarized in Table 2, including parameters such as moisture content, volatile matter, carbon content, and specific surface areas before and after KOH activation. The biomass produced has low moisture and ash content, but a significant percentage of volatile matter. It is important to note that the physical properties and composition of the biomass play a key role in the conversion of lignocellulosic material into activated carbon. The low moisture content (5%) suggests that the activated carbon may have high latent heat, while the low ash content (5.74%) indicates a predominantly organic composition, mainly carbon. The high volatile matter content (68.05%) suggests a high degree of graphitization in the activated carbon, resulting in an aromatic biochar with lower density [13]. These results suggest that charcoal derived from argan nuts is an excellent precursor for producing activated carbon. A closer examination of these data reveals that the activated carbon produced from this specific biomass source possesses unique characteristics, making it highly suitable for a variety of applications.

To evaluate the specific area of ArS AC and ArS BC, the Brunauer-Emmett-Teller (BET) approach was used before and after KOH activation. Before activation, the specific surface area was 212 m²/g, which increased significantly to 1665 m²/g after activation. This increase suggests

structural changes within the biochar upon KOH activation, likely resulting in the creation of additional pores or modification of existing pore structures. These changes may enhance the ability of biochar to interact with other substances by physical and chemical means [11].

Batch experiments: Response surface methodology

Study of the parameters: Statistical study

A total of 15 experiments were conducted under various experimental conditions, following the design proposed by the JMP software. This design was intended to minimize experimental errors and provide a robust framework for analyzing the interactions between different parameters. A randomized design with three central points was implemented to ensure the validity of the results. The data collected from these experiments are summarized in Table 3. Variance analysis was performed to interpret the results effectively, and statistical tests were used to calculate factor coefficients, examine their interactions, and determine their significance.

Factors considered in these tests include pH (X_1), the mass of ArS BC or ArS AC (X_2), and concentrations (X_3), with temperature, stirring speed, and contact time kept constant. The percentage removal results are presented in the table. To establish the relationship between the response

Table 2. Characterization of ArS and specific surface areas of ArS BC and ArS AC

Parameters	$H_{(ArS)}\%$	$Vm_{(ArS)}\%$	$C_{(ArS)}\%$	Specific surface area of ArS BC (m ² /g)	Specific surface area of ArS AC (m ² /g)
Results	5	68.05	5.74	212	1665

Table 3. Central surface design matrices for the study of adsorption

Unity	pH	Mass (g/L)	[Cr ⁶⁺] (pmm)	R% ArS BC	R% ArS AC
N°Exp					
1	6	0.6	50	14.9	39.65
2	4	0.2	50	20.08	65.48
3	4	1	50	38.99	97.91
4	4	0.6	30	27.88	87.75
5	6	1	30	21.366	74.77
6	6	0.2	30	10.033	49.7
7	2	0.6	50	30.84	97
8	4	0.2	10	34.65	95.3
9	2	1	30	39.667	99.21
10	2	0.6	10	45.002	99.5
11	2	0.2	30	35.66	96.7
12	4	0.6	30	27.02	87.03
13	4	0.6	30	28.74	88.32
14	6	0.6	10	39.254	90.25
15	4	1	10	47.5	100

variable Y and the three independent variables, including all their interactions, a second-order linear polynomial equation was used. The general form of the quadratic model is described by the following equation [34]:

$$Y = a_0 + b_1X_1 + b_2X_2 + b_3X_3 + b_{11}(X_1)^2 + b_{22}(X_2)^2 + b_{33}(X_3)^2 + b_{12}(X_1X_2) + b_{13}(X_1X_3) + b_{23}(X_2X_3) \quad (18)$$

where: a_0 represents the constant term, b_i denotes the linear interaction coefficients, b_{ii} signifies the quadratic interaction coefficients, the variables X_i (where $i = 1, 2, 3$) refer to the independent process factors, and Y indicates the parameter measured.

All the analyses were conducted using JMP software, a tool that facilitates optimal experimental strategy design and data analysis [35]. The optimal regression equations derived from the polynomial models indicate that positive parameter values (e.g., X_2 , X_1X_2 , X_1X_3 , X_2^2 , and X_3^2 for BC , and X_2 , X_1^2 , and X_3^2 for AC) result in a synergistic effect on Cr(VI) removal efficiency, while negative values suggest an inverse impact on Cr(VI) removal efficiency [35].

$$Y_{ArSBC} = 27.88 - 8.2017X_1 + 5.8875X_2 - 7.699X_3 - 2.0025X_1^2 + 0.8041X_2^2 + 6.621X_3^2 + 1.831X_1X_2 - 1.515X_1X_3 - 2.548X_2X_3 \quad (19)$$

$$Y_{ArSAC} = 87.7 - 17.26X_1 + 8.08X_2 - 10.63X_3 - 7.85X_1^2 + 0.225X_2^2 + 1.747X_3^2 + 5.622X_1X_2 - 12.025X_1X_3 + 6.93X_2X_3 \quad (20)$$

Correlation coefficient

The simulated values correlated with experimental values are illustrated in Figure 5, where the data points align closely along a straight line

[36]. This alignment indicates that the residuals satisfy the normality condition, For the model, the R^2 values were performed at 0.92 for ArS BC and 0.99 for ArS AC, indicating that 92% and 99% of the model determined can be expected to provide an explanation for the response variability of the response to Cr (VI) ion removal.

Furthermore, the model exhibits very high values for both the correlation coefficient and the adjusted R^2 values confirming the robustness of the predictions. Additionally, the low root mean square error (RMSE) values of 5.0358 for ArS BC and 3.7827 for ArS AC, further confirm that the model effectively describes the process under investigation [37].

Analysis of variance (ANOVA)

The variance analysis (ANOVA) assesses whether the selected variables significantly influence the responses of the two adsorbents, ArS BC and ArS AC [21]. A high value in this analysis suggests that the variation in response can be attributed to the regression equation. The corresponding p-values further substantiate the findings of the Fisher test. Both p-values are less than 0.05, with $p_{ArSBC} = 0.025$ as well as $p_{ArSAC} = 0.0004$. Therefore, these results indicate that there is no significant difference between the experimental values and the predicted values generated by the models [37]. Squared models are based on statistic values of significance provided by the R-squared ratio (R^2). The coefficient of determination (R^2), which represents the squared value of the linear correlation factor r , is one of the key indicators. Other indicators such as the root mean square error, average yield, and the probability of adjustment ($\text{prob} > F$) are also used [38]. The

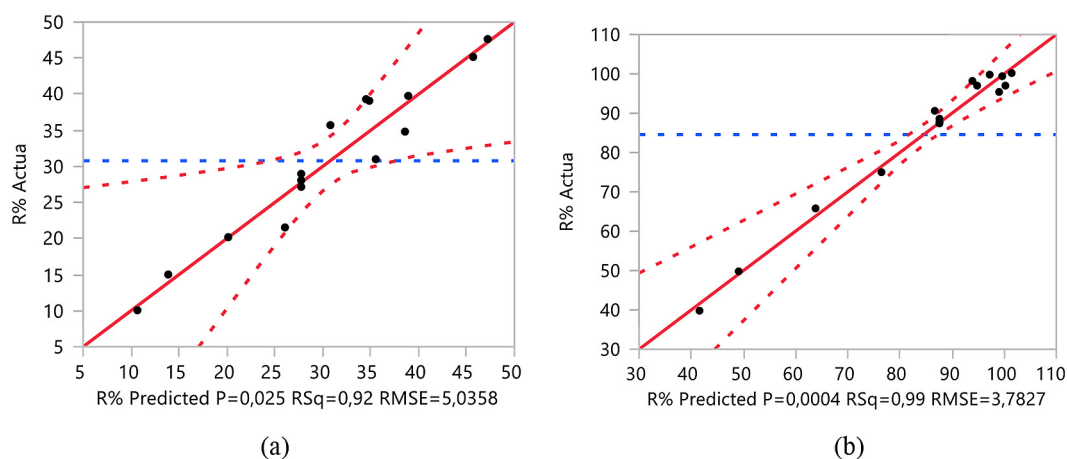


Figure 5. Observed and predicted chromium adsorption results of (a) ArS BC and (b) ArS AC

statistical indicators are given bellow. The determination factor ($R^2 = 0.999$) is considered satisfactory, indicating a high relationship between the predicted and fitted experimental values of the fitted modelling for both media [39].

Parameter optimization was performed using the desirability-based response surface methodology (RSM). This method provides an optimal fit, assessed on a scale ranging from 0 (poor performance) to 1 (optimal performance) (Table 4).

Effect of adsorption parameters

The analysis of the p-value indicates that the pH value (X_1), the mass of the adsorbent (X_2), and the initial concentration of the metal anion (X_3) significantly affect the quantity adsorbed by the biochar with a probability value of less than 0.05. Similarly, for activated carbon, the pH value (X_1), the mass of adsorbent (X_2), and the initial concentration of the metal anion (X_3), are significant factors influencing the quantity adsorbed. The quadratic terms (X_1^2), (X_2^2), (X_3^2), and their interaction term (X_1X_2) also demonstrate a notable influence. Based on the results obtained using JMP

software, the predictive equations are presented in Equations 21 and 22:

$$Y_{ArSBC} = 27.88 - 8.20175X_1 + - 5.88X_2 - 7.699X_3 \tag{21}$$

$$Y_{ArSAC} = 87.7 - 17.26X_1 + 8.08X_2 - - 10.63X_3 - 7.85X_1^2 + 0.225X_2^2 + + 1.747X_3^2 + 5.622 X_1X_2 \tag{22}$$

From the data presented in Table 5, the initial concentration negatively impacts the Cr(VI) removal rate for both ArS BC and ArS AC. This observation can be explained by the availability of surface sites on the adsorbents and the adsorbate-to-adsorbent ratio. At higher initial concentrations, the active sites of the adsorbents are surrounded by more Cr(VI) molecules in solution, which facilitates the adsorption process[40]. The mass of the adsorbent positively influences the Cr(VI) removal rate (%) for both ArS BC and ArS AC. As the mass of the adsorbent increases, the removal rate rises accordingly. This is due to the greater number of sorption sites provided by the larger adsorbent mass, allowing metal anions to access these sites more efficiently. Consequently,

Table 4. Variance analysis of the quantity of chromium adsorbed by ArS BC and ArS AC

Source	Degrees of freedom		Sum of squares		Mean square		F Ratio		
	ArS BC	ArS AC	ArS BC	ArS AC	ArS BC	ArS AC	ArS BC	ArS AC	
Model	9	9	1524.392	4956.6	169.377	550.729	6.6791	38.4886	
Error	5	5	126.796	71.544	25.359	14.309	Prob > F	Prob > F	
C. Total	14	14	1651.187	5028.1	-	-	0.025*	0.0004*	
Statistical factors									
R square		R square adj		Lack of fit		Root mean squared error		Mean of response	
ArS BC	ArS AC	ArS BC	ArS AC	ArS BC	ArS AC	ArS BC	ArS AC	ArS BC	ArS AC
0.92	0.985	0.785	0.960	0.9991	0.9998	5.0357	3.78	30.772	84.567

Table 5. Coefficient estimator by ANOVA study

Parameter	ArS BC				ArS AC			
	Estimate	Std error	t Ratio	Prob> t	Estimate	Std Error	t Ratio	Prob> t
Constante	27.88	2.907	9.59	0.0002*	87.7	2.184	40.16	<.0001*
pH(2,6)	-8.2017	1.780	-4.61	0.0058*	-17.26	1.337	-12.91	<.0001*
m(0.2,1)	5.8875	1.780	3.31	0.0213*	8.08	1.337	6.04	0.0018*
[Cr ⁶⁺](10,50)	-7.6993	1.780	-4.32	0.0075*	-10.63	1.337	-7.95	0.0005*
pH*m	1.8315	2.518	0.73	0.4996	5.62	1.89	2.97	0.0311*
pH*[Cr ⁶⁺]	-2.5485	2.518	-1.01	0.3579	-12.025	1.89	-6.36	0.0014*
m*[Cr ⁶⁺]	1.515	2.518	0.60	0.5736	6.93	1.89	3.67	0.0145*
pH*pH	-2.0025	2.621	-0.76	0.4793	-7.85	1.968	-3.99	0.0105*
m*m	0.804	2.621	0.31	0.7714	0.225	1.968	0.11	0.9135
[Cr ⁶⁺]*[Cr ⁶⁺]	6.621	2.621	2.53	0.0528	1.747	1.968	0.89	0.4154

the increased availability of binding sites on the surfaces of ArS BC and ArS AC enhances the quantity of adsorbates removed per unit mass of adsorbent [41]. Additionally, it was observed that the adsorption response increased as the pH decreased, with minimal adsorption occurring at higher pH levels (Figure 6). The functional groups on the surfaces of ArS BC and ArS AC, such as hydroxyl and carboxyl groups, impart an overall positive charge to biochar. Conversely, hexavalent chromium exists in anionic forms in solution, including HCrO_4^- , $\text{Cr}_2\text{O}_7^{2-}$, $\text{Cr}_3\text{O}_{10}^{2-}$, and $\text{Cr}_4\text{O}_{13}^{2-}$, at pH values ranging from 2 to 4 [42]. Thus, the adsorption involved in this study seems to be essentially due to an electrostatic attraction phenomenon. Furthermore, the adsorption capacity decreases as the pH increases. At higher concentrations, the availability of active sites decreases due to saturation by Cr(VI) molecules. Conversely, increasing the adsorbent mass positively affects removal efficiency by providing more sorption sites.

Parameters optimization

To determine the optimum conditions to maximize the adsorption of chromium by ArS BC and ArS AC, we used desirability-based numerical optimization to identify the best parameter values. The prediction profiler played an important role in selecting the optimal values for pH, mass of adsorbent and initial concentration of chromium, in order to obtain the highest possible removal efficiency. Figure 6a shows that, by maximizing the adsorption desirability of ArS BC, we obtained the following optimum conditions: an adsorbent dosage of 1 g/L, a pH 3 and a Cr^{6+} initial concentration equal to 10 mg/L. Under these conditions, with a desirability value close to 1, the maximum chromium adsorption reached 48.77%. Similarly Figure 6b indicates that, for ArS AC, the optimal conditions were a pH of 3, an adsorbent dosage of 0.6 g/L, and an initial chromium concentration of 50 mg/L. With a desirability value close to 1, the maximum chromium adsorption under these conditions reached 91.34%. The prediction profiler clearly

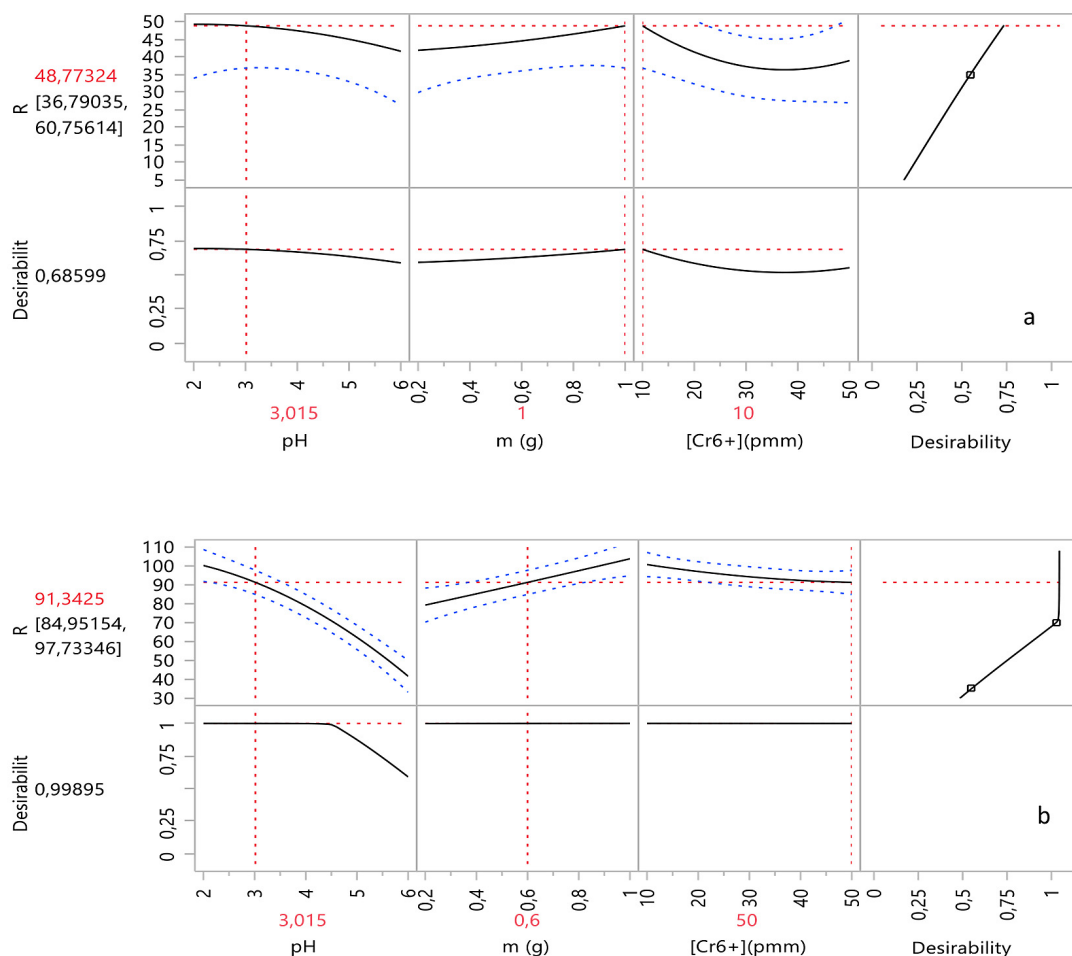


Figure 6. Cr(VI) Optimal conditions and expected Cr(VI) removal yields: (a) for ArS BC and (b) for ArS AC

demonstrates that the three parameters, pH, initial concentration, and adsorbent dosage, significantly influence the chromium adsorption rate.

Kinetic study of adsorption

Effect of time

The effect of contact time on Cr (VI) adsorption was examined over durations ranging from 5 to 300 minutes through two separate experiments conducted under controlled conditions. In the first experiment, a dose of 1 g/L of ArS BC was used with a pH of 3 and an initial Cr⁶⁺ concentration of 10 mg/L. In the second experiment, a dose of 0.6 g/L of ArS AC was applied, maintaining the same pH of 3 and an initial Cr⁶⁺ concentration of 50 mg/L. Variations in adsorption capacity are illustrated in Figure 7. A rapid increase in the removal rate occurred during the first few minutes for ArS AC, while for ArS BC, this increase extended over the first 60 minutes. A slower increase followed, up to 120 minutes for ArS AC and 180 minutes for ArS BC, eventually stabilizing. Figure 7 shows a Cr(VI) removal rate of 95.16% in 120 minutes for ArS AC, corresponding to an adsorption capacity of 101.64 mg/g. In contrast, ArS BC achieved a removal rate of 37.5% in 180 minutes, equivalent to an adsorption capacity of 22.5 mg/g. These results indicate that once equilibrium is reached, the adsorbent surface becomes saturated, limiting further adsorption.

Kinetic study of adsorption: kinetic models

To investigate the kinetics of chromium adsorption onto ArS BC and ArS AC, two kinetic models were employed: the pseudo-first-order model and the pseudo-second-order model. These models examined the adsorption mechanism and calculated the kinetic constants related to these processes.

The outcomes of the kinetic models are illustrated in Figure 8 and Table 6 presents the kinetic constants K_1 and K_2 , along with the calculated q_e values from both models. It also includes the coefficient of determination R^2 to evaluate how well the models fit the experimental data. The linear plots for the pseudo-first-order and pseudo-second-order models show linear relationships, with satisfactory correlation coefficient for pseudo-second-order models. Notably, the q_e values predicted by the pseudo-second-order model (11.11 mg/g for ArS BC and 90.91 mg/g for ArS AC) closely match the experimental adsorption values (10.38 mg/g for ArS BC and 84.32 mg/g for ArS AC), whereas the values derived from the pseudo-first-order model are lower than the experimental data. The comparison between ArS BC and ArS AC highlights that ArS AC exhibits a much higher adsorption capacity ($q_{e,exp} = 84.32$ mg/g) than ArS BC ($q_{e,exp} = 10.38$ mg/g), demonstrating the positive impact of chemical activation. However, the rate constant K_2 for ArS BC (0.00644 min⁻¹) is higher than for ArS AC (0.00247 min⁻¹), indicating that ArS BC reaches equilibrium faster. Overall,

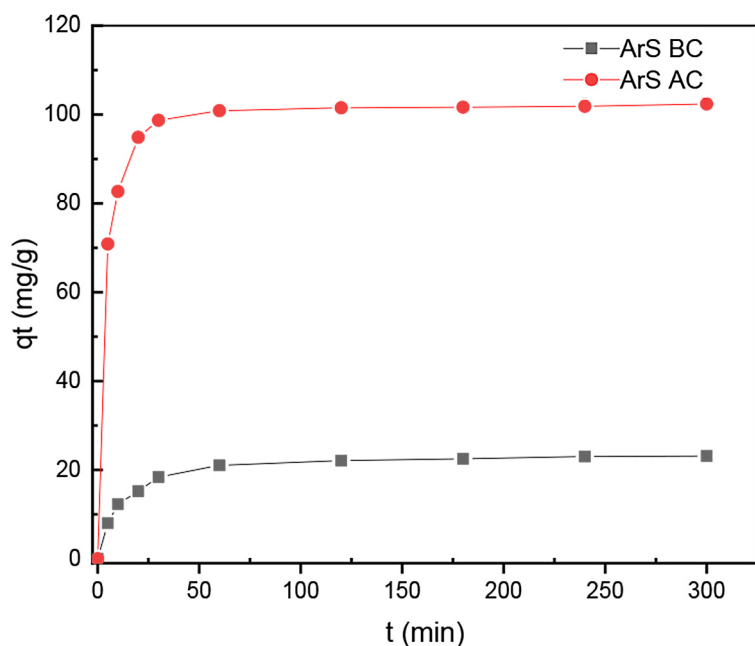


Figure 7. Contact time effect on Cr(VI) adsorption using ArS AC and ArS BC

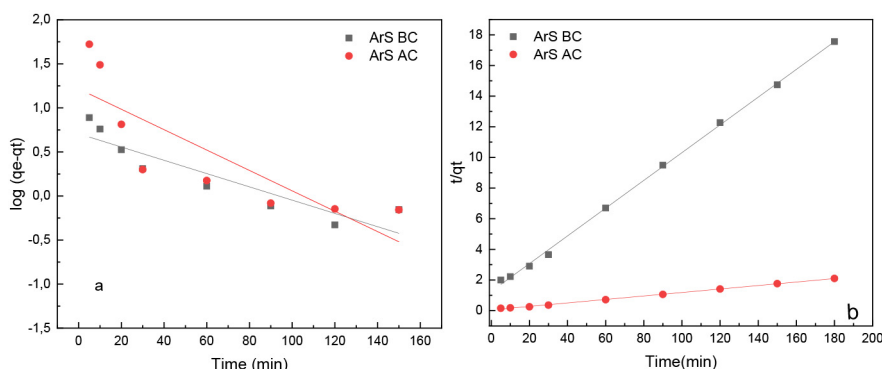


Figure 8. kinetic models: Pseudo-first order (a) and pseudo-second order (b) of ArS BC and ArS AC Cr⁶⁺ adsorption

Table 6. Pseudo-first-order and pseudo-second-order adsorption rate constants and experimental qe values for ArS BC and ArS AC

Parameter	Pseudo-First order				Pseudo-Second order			
	$q_{e,exp}$ (mg/g)	$q_{e,calculated}$ (mg/g)	K_1 (min ⁻¹)	R^2	$q_{e,exp}$ (mg/g)	$q_{e,calculated}$ (mg/g)	K_2 (min ⁻¹)	R^2
ArS BC	10.38	4.82	0.016	0.707	10.38	11.11	0.00644	0.999
ArS AC	84.32	16.44	0.027	0.646	84.32	90.91	0.00247	0.998

the pseudo-second-order model fits both systems best, suggesting that the adsorption process is controlled by chemical interactions between the adsorbate and the adsorbent [43].

Intra-particle diffusion

Using the Weber-Morris equation, the viability of Cr(VI) intraparticle movement in ArS BC and ArS AC was evaluated. The diffusion rate constants K_d were found by plotting qt as a function of $t^{1/2}$. Table 7 summarizes the results, including the correlation coefficient (R^2). Figure 9 illustrates the two separate stages of chromium adsorption on ArS BC and ArS AC. The high diffusion rate constants $k_{d1ArS BC}$ (7.645 mg.g⁻¹min^{-0.5}) and $k_{d1ArS AC}$ (8.268 mg.g⁻¹min^{-0.5})

in the initial phase, characterized by a steep slope, point to a quick adsorption process occurring on the materials' exterior surface. This stage is characterized by the fast adsorption of Cr(VI) onto the particle surface and the creation of a boundary layer. The high correlation coefficients ($R^2 = 0.938$ for ArS BC and $R^2 = 0.962$ for ArS AC) confirm the good fit of the kinetic models with the experimental data. In contrast, the diffusion rate constants $k_{d2 ArS BC}$ (0.021 mg.g⁻¹min^{-0.5}) and $k_{d2 ArS AC}$ (0.023 mg.g⁻¹min^{-0.5}), significantly decrease during the second phase, indicating a slowdown in the intra-particle diffusion process. This decrease, along with lower correlation coefficients ($R^2 = 0.951$ for ArS BC and $R^2 = 0.917$ for ArS AC), suggests that the

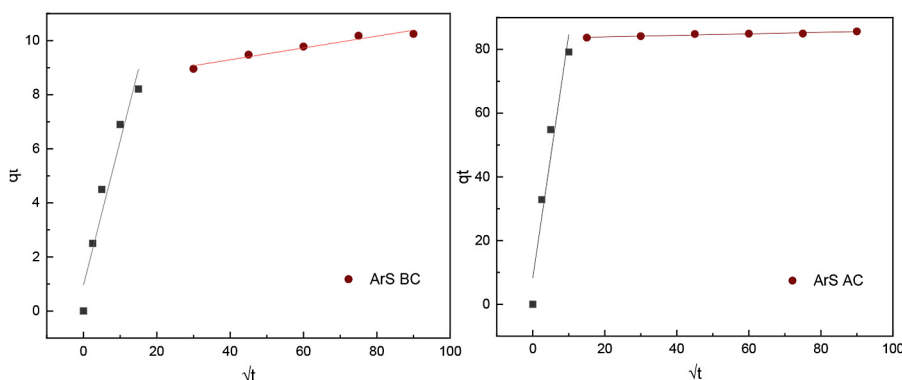


Figure 9. Two-stage intra-particle diffusion of chromium adsorption on ArS BC and ArS AC

Table 7. Intra-particle diffusion rate constants and correlation coefficients for ArS BC and ArS AC

Kinetic models	Parameters		ArS BC/Adsorbat	ArS AC/Adsorbat
Diffusion intra-particle [16]	Type I	R^2	0.938	0.941
		$k_d(\text{mg}\cdot\text{g}^{-1}\cdot\text{min}^{-0.5})$	0.532	7.645
		C	0.962	8.268
	Type II	R^2	0.951	0.917
		$k_d(\text{mg}\cdot\text{g}^{-1}\cdot\text{min}^{-0.5})$	0.021	0.023
		C	26.2	83.47

intra-particle diffusion slows down as the system approaches ultimate adsorption equilibrium, which is attributed to the Cr(VI) concentration in the surrounding solution. Accordingly, the research demonstrates that Cr(VI) adsorption for both ArS BC and ArS AC follows a two-stage diffusion model. In this model, rapid external surface adsorption characterizes the first phase, while a gradual decline in intraparticle diffusion leads to equilibrium in the second phase.

Adsorption isotherms models

Table 8 present the adsorption isotherm parameters for Cr (VI) on ArS BC and ArS AC. For the two supports, the Langmuir equilibrium constants were calculated using plots of $1/q_e$ versus $1/c_e$. The Langmuir isotherm exhibits very high R^2 values: 0.999 for ArS AC and 0.99 for ArS BC, indicating an excellent fit to the experimental data. Additionally, the maximum adsorption capacities q_m calculated from the Langmuir model were 333.333 mg/g for ArS AC and 47.619 mg/g for ArS BC. The non-dimensional constant R_L was 0.247 for ArS BC and 0.0689 for ArS AC, both within the favorable adsorption range of $0 < R_L < 1$. The tendency of R_L values toward 0 suggests potentially irreversible adsorption at higher metal concentrations. In summary, the Langmuir model provides the best fit for describing chromium

adsorption on both ArS AC and ArS BC supports, as evidenced by the agreement between calculated and experimental values. This isotherm suggests that adsorption occurs in a monolayer.

Freundlich equilibrium constants were calculated by plotting $\log(q_e)$ versus $\log(C_e)$, consistent with the linear form of the Freundlich equation. For ArS AC and ArS BC, the Freundlich isotherm is an acceptable model to describe adsorption. The coefficient of determination (R^2) for ArS BC is 0.961, indicating a reasonable fit to the data, although slightly less accurate compared to ArS AC, which has an even higher R^2 of 0.986. However, these R^2 values remain below the ideal value of 1 and are lower than those obtained with the Langmuir model. The values of $1/n$ are less than 1, indicating favourable adsorption for both supports. The Freundlich constant K_F , which evaluates adsorption capacity and surface heterogeneity, is 1.603 for ArS BC and 3.272 for ArS AC. These results suggest that adsorption on both ArS BC and ArS AC can be described by the Freundlich model, although the fit is slightly less precise for ArS BC than ArS AC [26].

The Temkin constant (K_T) is used in this model to evaluate the adsorbed molecules' interaction with the solid surface. The higher K_T value for activated carbon (1.61 L/mg) compared to biochar (0.17 L/mg) indicates that ArS AC has a stronger affinity for the adsorbate than ArS BC.

Table 8. Adsorption isotherm parameters for Cr (VI) on ArS BC and ArS AC

Parameter	Isotherm models	Factors			
ArS BC	Langmuir	$q_m = 47.6 \text{ mg/g}$	$K_L = 0.03034 \text{ mg/g}$	$R_L = 0.247$	$R^2 = 0.990$
	Freundlich	$K_F = 1.603 \text{ mg}^{1-n} \text{ L}^n/\text{g}$	$1/n = 0.653$	$n = 1.531$	$R^2 = 0.961$
	Temkin	$K_T = 0.17 \text{ L/mg}$	$B_T = 42.74 \text{ KJ/mol}$	-	$R^2 = 0.966$
	Dubinin-Radouchkevitch	$q_m = 28.13 \text{ mg/g}$	$E = 6.0912 \text{ kJ/mol}$		$R^2 = 0.967$
ArS AC	Langmuir	$q_m = 333.333 \text{ mg/g}$	$K_L = 0.111 \text{ mg/g}$	$R_L = 0.247$	$R^2 = 0.999$
	Freundlich	$K_F = 3.27199 \text{ mg}^{1-n} \text{ L}^n/\text{g}$	$1/n = 0.696$	$n = 1.4367$	$R^2 = 0.986$
	Temkin	$K_T = 1.61 \text{ L/mg}$	$B_T = 45.14 \text{ KJ/mol}$	-	$R^2 = 0.955$
	Dubinin-Radouchkevitch	$q_m = 146.057 \text{ mg/g}$	$E = 8.2788 \text{ kJ/mol}$		$R^2 = 0.971$

The average adsorption energy per molecule is represented by the Temkin parameter (B_T), with values of 42.74 kJ/mol for ArS BC and 45.14 kJ/mol for ArS AC. These relatively high values suggest that the adsorption process releases a significant amount of energy when molecules bind to the adsorbent surface, reinforcing the strong adsorbate-adsorbent interaction. The high correlation coefficients ($R^2 = 0.966$ for ArS BC and $R^2 = 0.955$ for ArS AC) indicate that the Temkin model provides a good fit to the experimental data. This confirms that adsorption is a well-defined phenomenon for both materials, with notable molecule-surface interactions [26]. In conclusion, the Temkin model effectively describes the observed adsorption process, with ArS AC exhibiting stronger adsorptive interactions compared to ArS BC.

The performance of chromium adsorption using the Dubinin-Radushkevich model demonstrates high maximum adsorption capacities (q_m) for both materials. ArS BC has an adsorption energy (E) of 6.0912 kJ/mol, which is below 8 kJ/mol, indicating that the adsorption of Cr(VI) on ArS BC occurs via physical adsorption. In contrast, the adsorption energy of ArS AC is 8.2788 kJ/mol, placing it within the 8–16 kJ/mol range, which suggests that Cr(VI) adsorption on ArS AC involves ion exchange. This implies that a moderate amount of energy is released when the molecules bind to the surface. The Dubinin-Radushkevich model exhibits a strong fit to

the experimental data, reinforcing its validity in describing the adsorption process for both materials [5].

The R^2 values of the adsorption models: Freundlich, Langmuir, Temkin, and Dubinin-Radushkevich, help determine the most suitable model for describing Cr (VI) adsorption on ArS BC and ArS AC. For ArS BC, the Langmuir model provides the best correlation with experimental data, followed closely by the Dubinin-Radushkevich model, indicating their strong relevance in describing the adsorption process. In contrast, the Freundlich model has the lowest R^2 value, suggesting it is the least accurate in fitting the experimental data. For ArS AC, the Langmuir model also offers the best fit, with the Freundlich model as a close second, while the Dubinin-Radushkevich model also shows a good correlation. However, the Temkin model has the lowest R^2 value, indicating a weaker fit. Overall, selecting the most suitable adsorption model depends on both theoretical relevance and the accuracy of the fit to experimental data in each specific study [26, 42].

Adsorption thermodynamic study

The various thermodynamic factors of the reaction, namely ΔG° , ΔH° , and ΔS° , allow for the evaluation of the spontaneity, feasibility, and nature of the adsorption. Calculations using

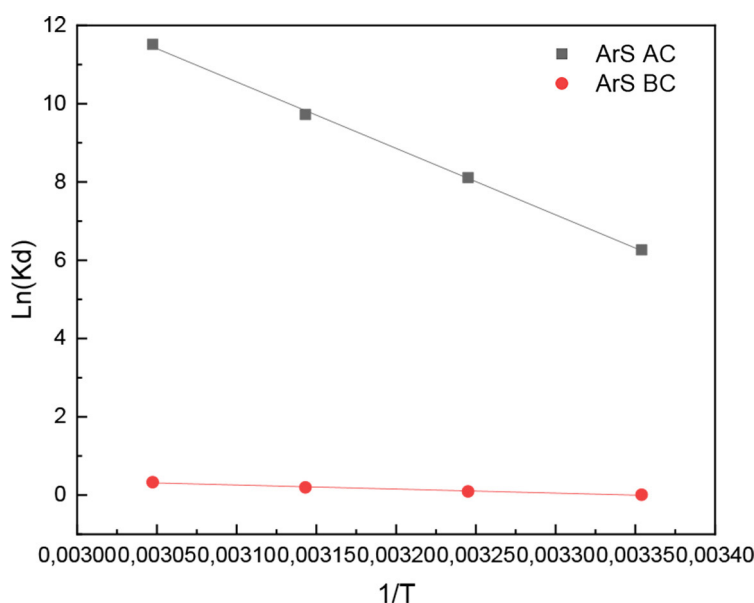


Figure 10. Variation of $\ln(K_d)$ as a function of $1/T$ for the calculation of ΔH° and ΔS° for ArS BC and ArS AC

Equations 23 and 24 provide these parameters (Figure 10) [44].

$$\ln(K_d) = \Delta S_o/R - \Delta H_o/RT \quad (23)$$

$$\Delta G_o = -RT \ln(K_d) \quad (24)$$

where: T is the temperature in Kelvin, R is the gas constant, and K_d can be obtained from q_e/C_e . ΔH_o and ΔS_o can be obtained from plotting $\ln(K_d)$ as a function of $1/T$.

The temperature range studied extended from 25 to 55 °C, using 30 mg of ArS AC and 50 mg of ArS BC. The adsorption capacity of Cr (VI) increased with temperature, rising from 99.68 to 100.01 mg/g for ArS AC and from 30.13 to 34.88 mg/g for ArS BC indicating an exothermic process [44]. Table 9 summarizes the thermodynamic parameters. The negative values of ΔG° confirm the spontaneous nature of Cr(VI) adsorption on both ArS AC and ArS BC. As shown in Table 9, ΔG° decreases with increasing temperature, reinforcing the feasibility of the process. The positive ΔH° reflects the endothermic nature of the adsorption, while the positive ΔS° values suggests increased disorder at the solid-liquid interface during the adsorption of Cr(VI) onto both ArS AC and ArS BC[44].

Comparison of chromium adsorption capacities on different adsorbents

To compare the various adsorbents listed in this Tables 10, 11 and 12, we first examine their adsorption capacities for Cr(VI). A higher adsorption value indicates greater efficiency in removing Cr(VI) from solution.

Among the biochars, ArS BC exhibits the highest adsorption capacity (47.6 mg/g), whereas apple biochar and eucalyptus tree bark biochar show significantly lower values (7.71 mg/g and 7.86 mg/g, respectively). Next, we consider the origin of the adsorbents. Some biochars are made from agricultural or forestry waste, while others may be synthetic materials or industrial residues. For example, wheat straw biochar (BCS), wheat straw biochar (BCW) and *Chlorella* sp. biochar are all biological materials, while landfill leachate (LLS) is a residue from landfill sites. pH is a critical factor influencing adsorption efficiency. Some adsorbent substances may perform better in acidic or alkaline environments. Most adsorbents in the literature were tested at pH 2. In this study, ArS BC, was evaluated at pH 3. This may suggest that the adsorbents are different

Table 9. Thermodynamic factors of Cr⁶⁺ adsorption onto ArS AC/ArS BC

Parameter	T	ΔG (KJ.mol ⁻¹)	ΔH (KJ.mol ⁻¹)	ΔS (J/mol*K)	R ²
ArS BC	298.15	-0.02148323	8.61	28.84	0.984
	308.15	-0.23928999			
	318.15	-0.52188931			
	328.15	-0.89554246			
ArS AC	298.15	-15.5242236	141.15	525.28	0.999
	308.15	-20.7806855			
	318.15	-25.7132358			
	328.15	-31.4100225			

Table 10. Comparison of Cr (VI) capacities on different biochar adsorbents

Samples	Adsorption capacity (mg/g)	S _{BET}	T °C	pH	Reference
Wheat straw biochar (BCS)	24.6	26.3	25 °C	2	[45]
Wheat wicker biochar (BCW)	23.6	11.4	25 °C	2	[45]
Eucalyptus bark biochar (EBB)	21.3	265	30 °C	2	[46]
Landfill leachate sludge (LLS)	17.46	83.87	25 °C	2	[7]
Eucalyptus tree bark biochar (BC)	7.86	48.4	-	9.31	[47]
Apple wood	7.71	0.0921	-	2	[1]
<i>Chlorella</i> sp. biochar	15.94	266	-	2	[48]
ArS BC	47.6	212	25 °C	3	[This work]

in terms of their sensitivity to pH variation, likely due to variations in surface functional groups and charge distribution. Notably, ArS BC stands out not only for its high adsorption capacity but also for its significant specific surface area (212 m²/g), making it a highly effective material for reducing contaminants. Its exceptional potential for water purification and treatment is evident.

AC ArS also distinguished itself among the activated biochar samples with an adsorption capacity of 333.33 mg/g, surpassing all other tested biochars. Although KOH-activated corn straw has the highest specific surface area (2183.8 m²/g), its adsorption capacity of 116.97 mg/g is still lower than that of AC ArS. With a specific surface area of 1665 m²/g, ArS AC demonstrates that adsorption capacity does not solely depend on specific surface area. The pH of ArS AC is 3, while the majority of other samples have a pH of 2, except for KOH-activated corn stalks, which have a pH of 4.5. Despite this difference, ArS AC has a remarkable adsorption capacity, suggesting that its structure and chemical properties play a crucial role. ArS AC is undoubtedly the most effective of the tested activated biochars in terms of adsorption capacity, even surpassing those with higher specific surface areas. Its optimized porous structure and chemical properties

enhance adsorption, making AC ArS a particularly effective choice for applications requiring high adsorption capacity.

When compared to commercial activated carbons, ARS AC again exhibits superior adsorption performance. It achieves the highest adsorption capacity (333.33 mg/g), significantly outperforming ACI (241.55 mg/g, ~28% lower) and AC (154.56 mg/g, ~53.6% lower) [55]. While its BET surface area of 1665 m²/g contributes to its effectiveness, the BET values of other commercial activated carbons are not available for direct comparison. All samples were tested at pH 2, a condition favorable for Cr(VI) adsorption. The two commercial activated carbons (AC and ACI) were sourced from different suppliers on Taobao. AC was purchased from the Longxin Water Purification Material Shop in Gongyi City, while ACI came from the Hongshu Environmental Protection Factory Shop [55]. In comparison, ArS BC (non-activated biochar) exhibits an adsorption capacity of 47.6 mg/g, which is considerably lower than both ArS AC and the commercial activated carbons. Despite this, ArS BC still shows a noteworthy capacity for Cr(VI) removal, with a BET surface area of 212 m²/g. While not as efficient as the activated forms, ArS BC provides a promising alternative, particularly in its potential

Table 11. Comparison of Cr(VI) adsorption capacities on different activated carbon adsorbents by KOH

Samples	Adsorption capacity (mg/g)	S _{BET}	T °C	pH	Reference
KOH activated sawdust biochar	45.88	18.698	25 °C	2	[6]
KOH activated corn straw biochar	116.97	2183.8	25 °C	2	[49]
KOH-activated Douglas Fir (DFBC)	127.2	1 050	45 °C	2	[50]
KOH Activated carbon from corn stalks	89.5	565.8	-	4.5	[51]
NaOH Activated carbon Date Press Cake (DPC)	282.8	2025.9	25 °C	2	[52]
KOH activated carbon from soy straw (SSAC)	294.12	1800.8	-	2	[53]
Activated carbon derived from glucose and sodium dodecylbenzenesulfonate (ACS)	79.6	1491.2	25 °C	2	[54]
ArS AC	333.33	1665	25 °C	3	[This work]

Table 12. Comparison of Cr(VI) adsorption capacities on different commercial adsorbents

Samples	Adsorption capacity (mg/g)	S _{BET}	T °C	pH	Reference
ArS BC	47.6	212	25 °C	3	[This work]
ACI (commercial activated carbon)	241.55	-	-	2	[55]
AC (commercial activated carbon)	154.56	-	-	2	[55]

for enhancement through activation, which could further improve its performance. Despite the effectiveness of KOH-activated adsorbents, specific data on commercially available KOH-activated products for Cr(VI) removal remains limited. Most research focuses on laboratory-prepared adsorbents from specific biomasses, rather than on commercially available KOH-activated products.

Desorption and regeneration studies

The adsorption of Cr(VI) on ArS AC and ArS BC is significantly influenced by the pH of the solution, and desorbing Cr(VI) with acidic reagents, such as HCl at pH 3, proves challenging. During initial adsorption at pH 3, the adsorption capacity was higher for ArS AC (149.47 mg/g) compared to ArS BC (58.78 mg/g). After the first desorption cycle with 2 M NaOH, the adsorption capacity decreased, although ArS AC (138.65 mg/g) still showed higher capacity than ArS BC (49.92 mg/g). In cycles 3 and 4, the adsorption capacity of ArS AC remained relatively constant around 135.98 mg/g, while that of ArS BC continued to decline, reaching 29.68 mg/g. By the fifth cycle, adsorption capacity of ArS AC decreased to 128 mg/g. The amounts of Cr(VI) desorbed with 2 M NaOH were significantly lower than the amounts adsorbed in each cycle. For desorption, the quantities of Cr(VI) desorbed were measured for each cycle, showing a gradual decrease for both materials, with higher values

for ArS AC compared to ArS BC. In summary, while both materials exhibit high initial Cr(VI) adsorption, ArS AC's adsorption capacity is more stable over the cycles, whereas ArS BC's capacity decreases more rapidly. Desorption with 2 M NaOH demonstrates limited efficiency in recovering adsorbed Cr(VI) (Figure 11).

Adsorption mechanism

FTIR data reveal significant changes in functional groups after Cr(VI) adsorption. For hydroxyl groups (O-H), peaks appear at 3441.83 cm^{-1} for ArS BC and 3435.68 cm^{-1} for ArS AC before adsorption, shifting to 3440.60 cm^{-1} and 3431.50 cm^{-1} respectively after adsorption. This suggests interactions through hydrogen bonding or complexation with Cr(VI). Aliphatic groups (CH and CH₂) show peaks at 2926.33 cm^{-1} and 2862.57 cm^{-1} for ArS AC, and at 2923.04 cm^{-1} and 2857.89 cm^{-1} for ArS BC before adsorption. These shift to 2923.04 cm^{-1} and 2851.89 cm^{-1} after adsorption, indicating minor interaction with Cr(VI). Peaks corresponding to carbonyl and aromatic groups (C=O and C=C) are located at 1628.36 cm^{-1} for ArS BC and 1629.26 cm^{-1} for ArS AC before adsorption, shifting to 1616.89 cm^{-1} and 1622.40 cm^{-1} respectively after adsorption. The significant increase in peaks at 1628.36 cm^{-1} , 1629.26 cm^{-1} , and 1384 cm^{-1} highlights the involvement of oxygen-containing groups in Cr(VI) removal. Carbonyl groups may act as electron donors, forming

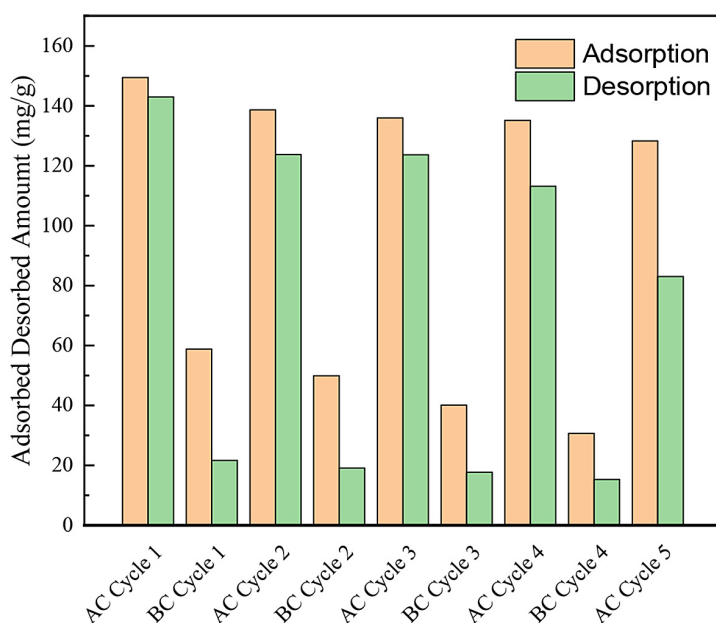


Figure 11. Adsorption-desorption cycles for repeated Cr⁶⁺ adsorption on ArS BC and ArS AC

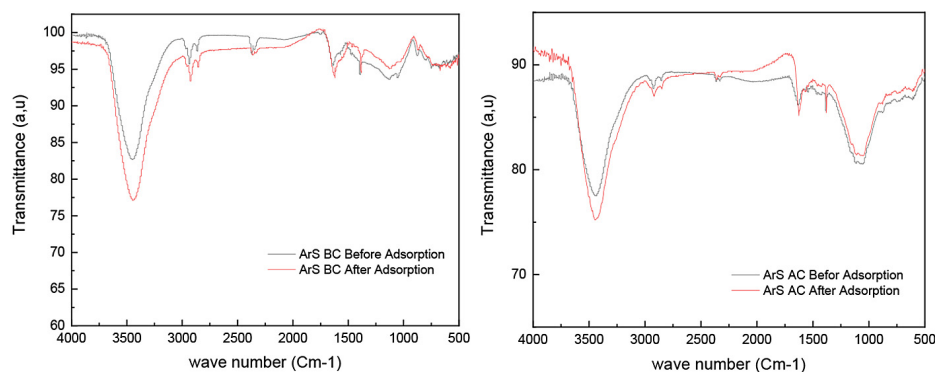


Figure 12. FT-IR analysis of ArS BC and ArS AC before and after Cr (VI) adsorption

stable complexes with chromium ions. Vibrations of alkoxy and aromatic groups (C-O) are observed at 1121.52 cm^{-1} and 1040.40 cm^{-1} for ArS BC, and at 1099.81 cm^{-1} for ArS AC before adsorption. After adsorption, these peaks shift to 1085.72 cm^{-1} and 1087.07 cm^{-1} , indicating strong interaction with Cr(VI), likely through complex formation [56]. FTIR analysis, combined with pH_{zpc} (point of zero charge) determination, provides crucial insights into adsorption mechanisms. The pH_{zpc} values, measured at 7.05 for biochar and 6.64 for activated carbon, indicate the pH at which the material surface has no net charge. Below these values, the protonation of hydroxyl and carboxyl functional groups causes the material surfaces to become positively charged, as confirmed by FTIR analysis (Figure 12).

CONCLUSIONS

In recent years, biochar and activated carbon have emerged as promising adsorbents for heavy metal removal due to their high surface area, porosity, and functional groups. In this study, we investigated the adsorption performance of argan shell biochar (ArS BC) and activated carbon (ArS AC) for Cr(VI) removal. The activation of biochar using KOH significantly enhanced its specific surface area, increasing it from $212\text{ m}^2/\text{g}$ to $1665\text{ m}^2/\text{g}$. The removal of Cr(VI) ions from an aqueous solution by ArS BC and ArS AC as adsorbents were evaluated using different kinetic models, isotherms as well as the RSM method. The findings reveal that, under optimal conditions namely, 1 g/L as adsorbent dosage, 3 for pH, and 10 mg/L as initial Cr(VI) concentration, ArS BC can achieve an adsorption rate of 48.77% for Cr(VI). In contrast, ArS AC demonstrated a higher

adsorption efficiency, with a rate of 91.34% under optimal conditions, which include a pH of 3 and 50 mg/L as initial concentration as well as 0.6 g/L for adsorbent dosage. The kinetic models demonstrated satisfactory correlation coefficients (R^2). The Langmuir equilibrium constants, with R^2 values of 0.999 for ArS AC and 0.99 for ArS BC, confirm the model's fit. The q_m values obtained were 333.333 mg/g for ArS AC and 47.619 mg/g for ArS BC. Moreover, the pseudo-second-order fits perfectly with the experimental results ($R^2 = 0.999$) and presents good adsorption data for Cr(VI). A key feature of these adsorbents is their recyclability: ArS BC can be reused for up to 4 cycles, while ArS AC can withstand 5 recycling cycles. This durability enhances the appeal of these materials for adsorption applications, offering a sustainable and cost-effective solution for water treatment.

REFERENCES

- Liu N. et al. (2019). Removal mechanisms of aqueous Cr(VI) using apple wood biochar: a spectroscopic study, *Journal of Hazardous Materials*, 384, 121371, 2020, <https://doi.org/10.1016/j.jhazmat.2019.121371>
- Tu B. et al. (2020). Efficient removal of aqueous hexavalent chromium by activated carbon derived from Bermuda grass, *Journal of Colloid and Interface Science*, 560, 649–658, <https://doi.org/10.1016/j.jcis.2019.10.103>
- Di Natale F., Lancia A., Molino A., and Musmarra D. (2007). Removal of chromium ions from aqueous solutions by adsorption on activated carbon and char, *Journal of Hazardous Materials*, 145(3), 381–390, <https://doi.org/10.1016/j.jhazmat.2006.11.028>
- Qu J. et al. (2021). KOH-activated porous biochar

- with high specific surface area for adsorptive removal of chromium (VI) and naphthalene from water: Affecting factors, mechanisms and reusability exploration, *Journal of Hazardous Materials*, 401, June 2020, 123292, <https://doi.org/10.1016/j.jhazmat.2020.123292>
5. Jimenez-Paz J., Lozada-Castro J. J., Lester E., Williams O., Stevens L., and Barraza-Burgos J. (2023). Solutions to hazardous wastes issues in the leather industry: adsorption of Chromium iii and vi from leather industry wastewaters using activated carbons produced from leather industry solid wastes, *Journal of Environmental Chemical Engineering*, 11(3), <https://doi.org/10.1016/j.jece.2023.109715>
 6. Zhang X., Zhang L., and Li A. (2018). Eucalyptus sawdust derived biochar generated by combining the hydrothermal carbonization and low concentration KOH modification for hexavalent chromium removal, *Journal of Environmental Management*, 206, 989–998, <https://doi.org/10.1016/j.jenvman.2017.11.079>
 7. Li Y. et al. (2022). Characteristics and adsorption of Cr(VI) of biochar pyrolyzed from landfill leachate sludge, *Journal of Analytical and Applied Pyrolysis*, 162, no. August 2021, <https://doi.org/10.1016/j.jaap.2022.105449>
 8. Babuji P., Thirumalaisamy S., Duraisamy K., and Periyasamy G. (2023). Human health risks due to exposure to water pollution: a review, *Water (Switzerland)*, 15(14), 1–15, <https://doi.org/10.3390/w15142532>
 9. Jamil U., Zeeshan M., Khan S. R., and Saeed S. (2023). Synthesis and two-step KOH based activation of porous biochar of wheat straw and waste tire for adsorptive exclusion of chromium (VI) from aqueous solution; thermodynamic and regeneration study, *Journal of Water Process Engineering*, 53, April, 103892, <https://doi.org/10.1016/j.jwpe.2023.103892>
 10. Ahmed R. et al. (2023). Activated carbon from sugarcane bagasse: a low-cost approach towards Cr(VI) removal from wastewater, *Chemistry (Switzerland)*, 5(2), 1124–1137, <https://doi.org/10.3390/chemistry5020077>
 11. Chen M., He F., Hu D., Bao C., and Huang Q. (2020). Broadened operating pH range for adsorption/reduction of aqueous Cr(VI) using biochar from directly treated jute (*Corchorus capsularis* L.) fibers by H₃PO₄, *Chemical Engineering Journal*, 381, no. July 2019, 122739, <https://doi.org/10.1016/j.cej.2019.122739>
 12. Al-Ahmed Z. A. et al. (2024). Facile synthesis of new metal-organic framework/chitosan composite sponge for Hg(II) removal: Characterization, adsorption efficiency, and optimization using Box-Behnken design, *International Journal of Biological Macromolecules*, 259, no. November 2023, <https://doi.org/10.1016/j.ijbiomac.2024.129282>
 13. Maazou S. D. B., Hima H. I., Malam Alma M. M., Adamou Z., and Natatou I. (2018). Elimination du chrome par du charbon actif élaboré et caractérisé à partir de la coque du noyau de Balanites aegyptiaca, *International Journal of Biological and Chemical Sciences*, 11(6), 3050, <https://doi.org/10.4314/ijbcs.v11i6.39>
 14. Najah EL Idrissi A., Benbrahim M., and Rassai N. (2023). Effect of the particle size argan nut shell (ANS) biomass on combustion parameters in stirring engine in Morocco, *Results in Engineering*, 18, no. May, 101202, <https://doi.org/10.1016/j.rineng.2023.101202>
 15. Genuino D. A. D., de Luna M. D. G., and Capareda S. C. (2018). Improving the surface properties of municipal solid waste-derived pyrolysis biochar by chemical and thermal activation: Optimization of process parameters and environmental application, *Waste Management*, 72, 255–264, <https://doi.org/10.1016/j.wasman.2017.11.038>
 16. Patra B. R., Nanda S., Dalai A. K., and Meda V. (2021). Taguchi-based process optimization for activation of agro-food waste biochar and performance test for dye adsorption, *Chemosphere*, 285, May, 131531, <https://doi.org/10.1016/j.chemosphere.2021.131531>
 17. Benadjemia M., Millièrè L., Reinert L., Benderdouche N., and Duclaux L. (2011). Preparation, characterization and Methylene Blue adsorption of phosphoric acid activated carbons from globe artichoke leaves, *Fuel Processing Technology*, 92(6), 1203–1212, <https://doi.org/10.1016/j.fuproc.2011.01.014>
 18. Hamri N. et al. (2024). Enhanced adsorption capacity of methylene blue dye onto kaolin through acid treatment: batch adsorption and machine learning studies, *Water (Switzerland)*, 16(2), 1–23, <https://doi.org/10.3390/w16020243>
 19. Haque S. M., Kabir A., Rahman N., and Azmi S. N. H. (2023). Response surface methodology combined Box-Behnken design optimized green kinetic spectrophotometric and HPLC methods to quantify angiotensin receptor blocker valsartan in pharmaceutical formulations, *Spectrochimica Acta - Part A: Molecular and Biomolecular Spectroscopy*, 298, April, 122805, <https://doi.org/10.1016/j.saa.2023.122805>
 20. Kouniba S., Benbiyi A., Zourif A., and EL Guendouzi M. Optimization use of watermelon rind in the coagulation-flocculation process by Box Behnken design for copper, zinc, and turbidity removal, *Heliyon*, 10(10), e30823, 2024, <https://doi.org/10.1016/j.heliyon.2024.e30823>
 21. Attia A. A., Khedr S. A., and Elkholly S. A. (2010).

- Adsorption of chromium ion (VI) by acid activated carbon, *Brazilian Journal of Chemical Engineering*, 27(1), 183–193, <https://doi.org/10.1590/S0104-66322010000100016>
22. Elkhilifi Z. et al. (2022). Lanthanum hydroxide engineered sewage sludge biochar for efficient phosphate elimination: Mechanism interpretation using physical modelling, *Science of the Total Environment*, 803, <https://doi.org/10.1016/j.scitotenv.2021.149888>
 23. Zulfiqar M., Samsudin M. F. R., and Sufian S. (2019). Modelling and optimization of photocatalytic degradation of phenol via TiO₂ nanoparticles: An insight into response surface methodology and artificial neural network, *Journal of Photochemistry and Photobiology A: Chemistry*, 384, May, 112039, <https://doi.org/10.1016/j.jphotochem.2019.112039>
 24. Khan M. N. et al. (2021). Remediation of emerging heavy metals from water using natural adsorbent: Adsorption performance and mechanistic insights, *Sustainability (Switzerland)*, 13(16), <https://doi.org/10.3390/su13168817>
 25. Ahmadou F., Abahdou F. Z., Slimani R., and El Hajjaji S. (2023). Kinetic, isotherm and thermodynamic studies on the adsorption of Methylene blue dye using Moringa oleifera pods and kernels, *Moroccan Journal of Chemistry*, 11(1), 265–281, <https://doi.org/10.48317/IMIST.PRSM/morjchem-v11i1.34864>
 26. Zhou Y., Li Y., Liu D., Liu D., Xu L., and Liu C. (2021). Adsorption optimization of uranium(VI) onto polydopamine and sodium titanate co-functionalized MWCNTs using response surface methodology and a modeling approach, *Colloids and Surfaces A: Physicochemical and Engineering Aspects*, 627, January, <https://doi.org/10.1016/j.colsurfa.2021.127145>
 27. Arrakhiz F. Z. et al. (2013). Mechanical and thermal properties of natural fibers reinforced polymer composites: Doum/low density polyethylene, *Materials and Design*, 43, 200–205, <https://doi.org/10.1016/j.matdes.2012.06.056>
 28. Dehkhoda A. M., Ellis N., and Gyenge E. (2014). file:///C:/Users/hp/Desktop/adsorption_chrome/s13762-019-02219-4.pdf, *Journal of Applied Electrochemistry*, 44(1), 141–157, <https://doi.org/10.1007/s10800-013-0616-4>
 29. Lazzari E. et al. (2018). Classification of biomass through their pyrolytic bio-oil composition using FTIR and PCA analysis, *Industrial Crops and Products*, 111, October 2017, 856–864, <https://doi.org/10.1016/j.indcrop.2017.11.005>
 30. Ibrahim W. M., Hassan A. F. and Azab Y. A. (2016). Biosorption of toxic heavy metals from aqueous solution by Ulva lactuca activated carbon, *Egyptian Journal of Basic and Applied Sciences*, 3(3), 241–249, <https://doi.org/10.1016/j.ejbas.2016.07.005>
 31. Klaai L., Hammiche D., Boukerrou A., and Ezzahra Arrakhiz F. (2022). Assessment of natural cellulosic fibers derived from agricultural by-product, *Materials Today: Proceedings*, 53, 260–264, <https://doi.org/10.1016/j.matpr.2022.01.088>
 32. Rattanawongkun P., Kerddonfag N., Tawichai N., Intatha U., and Soykeabkaew N. (2020). Improving agricultural waste pulps via self-blending concept with potential use in moulded pulp packaging, *Journal of Environmental Chemical Engineering*, 8(5), 104320, <https://doi.org/10.1016/j.jece.2020.104320>
 33. Liang M., Ding Y., Zhang Q., Wang D., Li H., and Lu L. Removal of aqueous Cr(VI) by magnetic biochar derived from bagasse, *Scientific Reports*, 10(1), 1–13, 2020, <https://doi.org/10.1038/s41598-020-78142-3>
 34. Lee S. M., Lalmhunsiamma, Il Choi S., and Tiwari D. (2013). Manganese and iron oxide immobilized activated carbons precursor to dead biomasses in the remediation of cadmium-contaminated waters, *Environmental Science and Pollution Research*, 20(10), 7464–7477, <https://doi.org/10.1007/s11356-013-1609-x>
 35. Tomasi I. T., Santos S. C. R., Boaventura R. A. R., and Botelho C. M. S. (2023). file:///C:/Users/hp/Desktop/adsorption_chrome/1-s2.0-S2213343718301490-main.pdf, *Journal of Cleaner Production*, 395, July 2022, <https://doi.org/10.1016/j.jclepro.2023.136452>
 36. Witek-Krowiak A., Chojnacka K., Podstawczyk D., Dawiec A., and Bubala K. (2014). Application of response surface methodology and artificial neural network methods in modelling and optimization of biosorption process, *Bioresource Technology*, 160, 150–160, <https://doi.org/10.1016/j.biortech.2014.01.021>
 37. Azzouni D., Baragh F., Mahmoud A. M., Alanazi M. M., Rais Z., and Taleb M. (2023). Optimization of methylene blue removal from aqueous solutions using activated carbon derived from coffee ground pyrolysis: A response surface methodology (RSM) approach for natural and cost-effective adsorption, *Journal of Saudi Chemical Society*, 27(5), 101695, <https://doi.org/10.1016/j.jscs.2023.101695>
 38. Es-said A., El hamdaoui L., El Moussaouiti M., and Bchitou R. (2019). Esterification optimization of cellulose with p-Iodobenzoyl chloride using experimental design method, *Journal of Polymer Research*, 26(9), <https://doi.org/10.1007/s10965-019-1862-x>
 39. Singh S., Chakraborty J. P., and Mondal M. K. (2020). Pyrolysis of torrefied biomass: Optimization of process parameters using response surface methodology, characterization, and comparison of properties of pyrolysis oil from raw biomass, *Journal*

- of *Cleaner Production*, 272, 122517, <https://doi.org/10.1016/j.jclepro.2020.122517>
40. Soliman N. K., Moustafa A. F., Aboud A. A., and Halim K. S. A. (2019). Effective utilization of Moringa seeds waste as a new green environmental adsorbent for removal of industrial toxic dyes, *Journal of Materials Research and Technology*, 8(2), 1798–1808, <https://doi.org/10.1016/j.jmrt.2018.12.010>
 41. Güray T., Menevşe B., and Yavuz A. A. (2020). Determination of optimization parameters based on the Box-Behnken design for cloud point extraction of quinoline yellow using Brij 58 and application of this method to real samples, *Spectrochimica Acta - Part A: Molecular and Biomolecular Spectroscopy*, vol. 243, 118800, <https://doi.org/10.1016/j.saa.2020.118800>
 42. Ghani U. et al. (2022). Adsorption of methyl orange and Cr (VI) onto poultry manure-derived biochar from aqueous solution, *Frontiers in Environmental Science*, 10, June, 1–13, <https://doi.org/10.3389/fenvs.2022.887425>
 43. Khezami L. and Capart R. (2005). Removal of chromium(VI) from aqueous solution by activated carbons: Kinetic and equilibrium studies, *Journal of Hazardous Materials*, 123(1–3), 223–231, <https://doi.org/10.1016/j.jhazmat.2005.04.012>
 44. Zhou X., Yu X., Maimaitiniyazi R., and Zhang X. (2023). Heliyon discussion on the thermodynamic calculation and adsorption spontaneity re Ofudje et al. *Heliyon*, 10(8), e28188, 2024, <https://doi.org/10.1016/j.heliyon.2024.e28188>
 45. Tytlak A., Oleszczuk P., and Dobrowolski R. (2015). Sorption and desorption of Cr(VI) ions from water by biochars in different environmental conditions, *Environmental Science and Pollution Research*, 22(8), 5985–5994, <https://doi.org/10.1007/s11356-014-3752-4>
 46. Choudhary B. and Paul D. (2018). Isotherms, kinetics and thermodynamics of hexavalent chromium removal using biochar, *Journal of Environmental Chemical Engineering*, 6(2), 2335–2343, <https://doi.org/10.1016/j.jece.2018.03.028>
 47. Yusuff A. S., Popoola L. T., and Igbafe A. I. (2022). [file:///C:/Users/hp/Desktop/adsorption chrome/1-s2.0-S0960852419308089-main.pdf](file:///C:/Users/hp/Desktop/adsorption%20chrome/1-s2.0-S0960852419308089-main.pdf), *Chemical Engineering Research and Design*, 182, 592–603, <https://doi.org/10.1016/j.cherd.2022.04.007>
 48. Amin M. and Chetpattanondh P. (2019). Biochar from extracted marine *Chlorella sp.* residue for high efficiency adsorption with ultrasonication to remove Cr(VI), Zn(II) and Ni(II), *Bioresource Technology*, 289, May, 121578, <https://doi.org/10.1016/j.biortech.2019.121578>
 49. Qu J. et al. (2021). KOH-activated porous biochar with high specific surface area for adsorptive removal of chromium (VI) and naphthalene from water: Affecting factors, mechanisms and reusability exploration, *Journal of Hazardous Materials*, 401, June, 123292, <https://doi.org/10.1016/j.jhazmat.2020.123292>
 50. Herath A., Layne C. A., Perez F., Hassan E. B., Pittman C. U., and Mlsna T. E. (2021). KOH-activated high surface area Douglas Fir biochar for adsorbing aqueous Cr(VI), Pb(II) and Cd(II), *Chemosphere*, 269, 128409, <https://doi.org/10.1016/j.chemosphere.2020.128409>
 51. Zhao J., Yu L., Ma H., Zhou F., Yang K., and Wu G. (2020). Corn stalk-based activated carbon synthesized by a novel activation method for high-performance adsorption of hexavalent chromium in aqueous solutions, *Journal of Colloid and Interface Science*, 578, 650–659, <https://doi.org/10.1016/j.jcis.2020.06.031>
 52. Norouzi S. et al. (2018). Preparation, characterization and Cr(VI) adsorption evaluation of NaOH-activated carbon produced from Date Press Cake; an agro-industrial waste, *Bioresource Technology*, 258, February, 48–56, <https://doi.org/10.1016/j.biortech.2018.02.106>
 53. Guo X., Hu W., Gu Z., Li J., Xie Z., Fang C., Tao H. (2021). Enhanced removal of aqueous chromium(VI) by KOH-activated soybean straw-based carbon, *Water Air Soil Pollut.* <https://doi.org/10.1007/s11270-021-05435-2>
 54. Xu H. et al. (2021). Science of the total environment adsorption of Cr (VI) from aqueous solutions using novel activated carbon spheres derived from glucose and sodium dodecylbenzene sulfonate, *Science of the Total Environment*, 759, 143457, <https://doi.org/10.1016/j.scitotenv.2020.143457>
 55. Wang H., Wang W., Zhou S., and Gao X. (2023). Adsorption mechanism of Cr(VI) on woody-activated carbons, *Heliyon*, 9(2), e13267, Jan. <https://doi.org/10.1016/j.heliyon.2023.e13267>
 56. Solgi M., Najib T., Ahmadnejad S., and Nasernejad B. (2017). Resource-Efficient Technologies Synthesis and characterization of novel activated carbon from Medlar seed for chromium removal : Experimental analysis and modeling with artificial neural network and support vector regression, *Resource-Efficient Technologies*, 3(3), 236–248, <https://doi.org/10.1016/j.refit.2017.08.003>